This paper appears in IEEE Transactions on Haptics, 2020, DOI 10.1109/TOH.2020.2983037

Design and Control of a 3 Degree-of-Freedom Parallel Passive Haptic Device

Maciej Łącki, and Carlos Rossa

***Abstract*—Teleoperated robotic surgery and surgical simulation provide surgeons with tools that can improve the health outcomes of their patients. The limiting factor in many of these systems, however, is the lack of a haptic system that can render high impedance without compromising transparency or stability. To address this issue, we constructed a 3-Degree-of-Freedom haptic device using brakes as actuators. A novel controller is also proposed to increase the range of forces the device can generate and eliminate stiction. The device uses a modified Delta kinematic structure making it light and rigid. Since brakes are intrinsically stable, the device safely generates a wide range of impedance making it well suited for many surgical applications.**

The novel controller attempts to minimize the sum of forces acting perpendicular to the virtual surface eliminating un-smooth force output and stiction characteristic to passive devices, while increasing the range of displayable forces. The controller was validated using six testing scenarios where it rendered contact with frictionless surfaces. When using the controller, the device rendered the desired surface without stiction. Since the controller successfully rendered complex geometry, it can also work in other applications, such as robotic surgery and surgical simulation.

***Index Terms*—Haptics, Force-Feedback, Passive, Brakes, 3-DOF, Parallel Kinematics, Force Controller**

I. Introduction

TELEOPERATED robotic surgery allows surgeons to complete difficult procedures with unparalleled accuracy. The majority of these systems, however, do not provide force-feedback to the user [1]. This isolates surgeons from the kinesthetic feedback they rely on when completing a task manually. Evidence suggests that providing force-feedback to the surgeons improves their performance and accuracy, while also making the robotic systems more intuitive to use [2]–[4].

Surgeons and medical students use surgical simulation to practice the manual skills necessary to complete surgical procedures without putting patients at risk of injury or even death. These simulators perform the same function as cadavers or animal phantoms used today, at a fraction of the cost [5]–[7]. These systems use haptic force-feedback devices (*haptic devices*, henceforth) to provide the user with the sensation that they would experience during a real surgery.

Fundamentally, a haptic device attempts to imitate the forces one would sense when interacting with a real or simulated environment. To achieve this, an ideal device should have no mass or inertia, and it should generate a wide range of impedance. In surgical applications, high impedance is required to accurately render hard tissues, bones, or virtual fixtures, while low impedance is needed to simulate contact with soft tissues, like organs and skin [8], [9].

Transparency of a haptic device, defined as the ratio of desired and applied impedance, is of utmost importance in surgical applications. Interaction of a tool, such as a needle, with tissue involves forces on the scale of mili-Newtons [9]. Such forces are often much smaller compared with the forces resulting from inertia or friction of the haptic device. The lack of transparency in haptic devices is currently considered to be one of the main issues in surgical simulation [10]–[13]. In fact, the friction introduced by a haptic device can cause surgeons to perform worse in force-feedback simulation, compared with the simulation without the force-feedback [10]. Additionally, unrealistic force feedback resulting, in part, from friction proved to have negative effects on the skill acquisition of the medical students [12].

Unfortunately, transparency has a detrimental effect on stability. As proven in [14], quantization of time and position causes instability when rendering a high impedance. There is, in fact, an intrinsic trade-off between the transparency and the stability of an active device. Thus, to render the environment with substantial impedance the device must experience substantial damping compromising its transparency.

Passive haptic devices (*passive devices*, hereafter), on the other hand, do not have this limitation. Instead of motors, these devices use brakes, which are intrinsically stable. This means that a passive device can generate high impedance without sacrificing its stability or transparency [15]–[18]. Brakes can also generate greater torque than an electric motor of the same volume and/or mass [19]–[21]. As a result, a passive device can be more transparent and generate a wider range of forces than a comparable active device, making it ideally suited for robotic surgery and simulation. Notably, passive devices are incapable of compensating for gravity or inertia, which makes the mass of the device perceivable to the user.

Passive devices are difficult to control. Unlike a motor, the direction of the force output in a passive device is uncontrollable since a brake generates forces to oppose its velocity [22]. As a result, only the magnitude of the force can be controlled, which means that a passive device cannot generate force in an arbitrary direction [23]. Additionally, moving brakes compared to stationary brakes produce different magnitudes of forces causing stiction, which has a detrimental effect on the accuracy and the realism of a rendered environment.

Maciej Łącki, and Carlos Rossa are with Faculty of Engineering and Applied Science at Ontario Tech University, Oshawa, Ontario, Canada. E-mail: maciej.lacki@OntarioTechU.net, carlos.rossa@OntarioTechU.ca

We acknowledge the support of the Natural Sciences and Engineering Research Council of Canada (NSERC), [funding number 2018-06074]. Cette recherche a été financée par le Conseil de recherches en sciences naturelles et en génie du Canada (CRSNG), [numéro de référence 2018-06074].

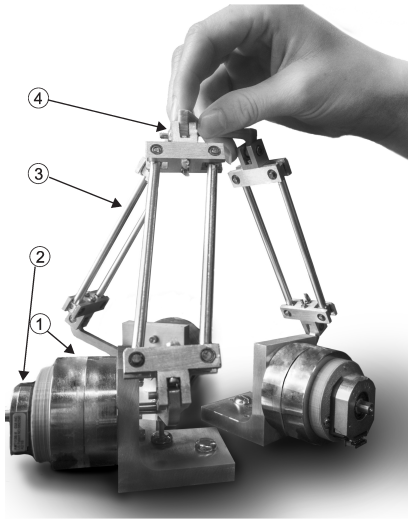

Fig. 1. The assembled device consists of 3 identical legs (3) attached to the end-effector (4). Each leg is actuated by a brake (1), and its angular position is measured using an encoder (2).

The majority of passive haptic devices developed through the years were constrained to 2 degrees-of-freedom (DOF). Surgical applications, however, require haptic devices with at least 3 translational DOF [24], [25]. To the best of our knowledge, there has only been one documented example of a passive haptic device with 3-DOF translational motion. This device was developed for dental implant surgery simulation and used a 5-bar regional kinematic structure, like the one in PHANToM devices [26]. The kinematic structure minimized the effects of gravity on the device but also introduced inertia [27]. Parallel kinematic structures, on the other hand, have lower inertia making them more transparent. Since transparency is a key issue in both surgical simulation and robotic surgery, a device using parallel kinematics can be well suited for the surgical applications.

In this paper, we present a passive haptic device with 3 translational DOF in Section II. Next, Section III models the force output of the device and use it to develop a novel controller in Section IV. This controller aims to alleviate the issues caused by brakes namely stiction and the uncontrollable direction of the force output. The performance of the controller is then tested in Section V and discussed in the context of surgical applications in Section VI. Finally, we review the results and determine whether the device and the controller are suitable for surgical applications in Section VII.

The controller developed for the passive device uses the paradigm of reference force to approximate a desired force. Like in [28], [29], the controller attempts to approximate the desired force by eliminating the normal component of the net force acting on the plane or surface rendered by the haptic device. Unlike the previous controllers, our approach is not limited to 2-DOF and is able to approximate desired forces using a combination of 1, 2, or all 3 available actuators. Let us start with the design of the 3-DOF Passive Haptic Device.

II. 3-DOF Parallel Passive Haptic Device

The 3-DOF device, shown in Fig. 1, uses a variation of the parallel kinematic structure known as the *Delta* configuration. This kinematic structure was chosen due its high rigidity, transparency, and lack of inefficient spherical joints, commonly found in other parallel manipulators. The device has only translational DOF, meaning that the end-effector remains parallel to the base at all times. By employing parallel kinematics the heavy brakes are fixed at the bottom platform reducing the mass of the moving parts, minimizing the apparent inertia of the device. Furthermore, the links of the device are made from aluminium, keeping the device light and rigid and each joint included a pair of bearings minimizing the joint friction.

The device is actuated by three Placid Industries B-2 magnetic particle brakes. The choice of these brakes is dictated by their wide torque range spanning from $8.5\,\text{mN}\cdot\text{m}$ (off-state torque) to $280\,\text{mN}\cdot\text{m}$ resulting in a max-to-min torque ratio of 32.9. The angular position of each brake is measured using an incremental encoder with a resolution of 2048 pulses-per-revolution (AMT112Q from CUI Inc.). Using the encoder data, the position of the device can be determined within $1.5\,\text{mm}$ accuracy. The device generates a peak force of approximately $10\,\text{N}$ when $\theta_{11} = \theta_{12} = \theta_{13} = 0.02$ rad satisfying the requirements for laparoscopic procedures [9]. Note, however, that for applications requiring higher force output other, stronger brakes can be used. To the best of our knowledge the modified Delta kinematic structure has never been used with passive actuators for haptic applications. The kinematic structure of the device includes 3 legs shown in Fig. 2(a), as well as top and bottom platforms, in Fig. 2(b) and Fig. 2(c) respectively. The link lengths of the device were chosen based on previously established designs, namely the Novint Falcon, and they are listed in Table I. Using these link lengths, it is possible to solve the inverse kinematics of the device.

A. Inverse Kinematics

In an inverse kinematics problem the joint angles of the device are calculated for a specified position of the end-effector $\mathbf{X}_{xyz}$ in the xyz fixed coordinate frame. To solve this problem it is convenient to independently consider each of the three legs composing the device. In Fig. 2(a), leg i has three defining angles, $\boldsymbol{\theta}_{1i}$, $\boldsymbol{\theta}_{2i}$, $\boldsymbol{\theta}_{3i}$. Each leg in the system is independent of the others, therefore, we can solve for the angle in each leg independent of any other leg. Let uvw_i represent the new reference frame for leg i defined such that u acts along the rotation axis of the brake at an angle ϕ_i from the original reference frame, like in Fig. 2(a). The position of the attachment point for each leg in the uvw_i reference frame, $\mathbf{X}_{uvw_i} = [U_i \quad V_i \quad W_i]$, is given by,

$$\begin{bmatrix} U_i \\ V_i \\ W_i \end{bmatrix} = \begin{bmatrix} \cos\phi_i & \sin\phi_i & 0 \\ -\sin\phi_i & \cos\phi_i & 0 \\ 0 & 0 & 1 \end{bmatrix} \begin{bmatrix} X_x \\ X_y \\ X_z \end{bmatrix} + \begin{bmatrix} -r \\ -s \\ 0 \end{bmatrix} \quad (1)$$

where $\phi_i = [0 \quad 2\pi/3 \quad 4\pi/3]$ corresponds to the angle between the base frame and link a of leg i [30]–[32].

In the new reference frame the end-effector position is:

$$U_i = a\,\cos\theta_{1i} - c + \cos\theta_{2i}\,(d + e + b\,\sin\theta_{3i}) \tag{2a}$$
$$V_i = b\,\cos\theta_{3i} \tag{2b}$$
$$W_i = a\,\sin\theta_{1i} + \sin\theta_{2i}\,(d + e + b\,\sin\theta_{3i}). \tag{2c}$$

Solving (2b) gives,

$$\theta_{3i} = \arccos\left(\frac{V_i}{b}\right). \tag{3}$$

Note that a positive and a negative solution to (3) exists but due to the physical constraints of the manipulator links, only the positive solution is possible [31], [32]. Similarly, only the positive solution is valid for θ_{1i}, found using

$$\theta_{1i} = \arcsin\left(\frac{2\,t_i}{1 + t_i^2}\right) \tag{4}$$

with

$$t_i = \frac{-l_i - \sqrt{l_i^2 - 4\,l_{2i}\,l_{0i}}}{2\,l_{2i}}$$

where $t_i \in \mathbb{R}$, and

$$\begin{aligned} l_{0i} =& W_i^2 + U_i^2 + 2cU_i - 2aU_i + a^2 + c^2 - d^2 - e^2 \\ & - b^2\sin^2\theta_{3i} - 2be\sin\theta_{3i} - 2bd\sin\theta_{3i} - 2de - 2ac \\ l_{1i} =& -4aW_i \\ l_{2i} =& W_i^2 + U_i^2 + 2cU_i + 2aU_i + a^2 + c^2 - d^2 - e^2 \\ & - b^2\sin^2\theta_{3i} - 2be\sin\theta_{3i} - 2bd\sin\theta_{3i} - 2de + 2ac. \end{aligned}$$

Knowing θ_{1i} and θ_{3i}, the last angle, θ_{2i}, is

$$\theta_{2i} = \arccos\left(\frac{W_i - a\,\sin\theta_{1i} - \sin\theta_{2i}}{d + e + b\,\sin\theta_{3i}}\right). \tag{5}$$

With all three angles in the three legs of the device known, it is possible to find the Jacobian matrix for the device.

B. Jacobian Matrix

The Jacobian of the manipulator relates angular velocity of the joints $\dot{\boldsymbol{\theta}}$ to the velocity of the end-effector in Cartesian space $\dot{\mathbf{X}}$ such that,

$$\dot{\mathbf{X}} = \mathbf{J}\,\dot{\boldsymbol{\theta}}. \tag{6}$$

The Jacobian is obtained by taking a partial derivative of the loop equations $\partial(U_i, V_i, W_i)/\partial(\theta_{11}, \theta_{12}, \theta_{13})$, and solving for the joint rates $\dot{\theta}_{11}, \dot{\theta}_{12}, \dot{\theta}_{13}$ resulting in,

$$\mathbf{J} = \begin{bmatrix} J_{11} & J_{12} & J_{13} \\ J_{21} & J_{22} & J_{23} \\ J_{31} & J_{32} & J_{33} \end{bmatrix} \tag{7}$$

where each element of the Jacobian is [30], [31]:

$$J_{1i} = \frac{\cos\theta_{3i}\,\sin\phi_i - \cos\phi_i\,\cos\theta_{2i}\,\sin\theta_{3i}}{a\,\sin(\theta_{1i} - \theta_{2i})\,\sin\theta_{3i}}$$
$$J_{2i} = -\frac{\cos\phi_i\,\cos\theta_{3i} + \cos\theta_{2i}\,\sin\phi_i\,\sin\theta_{3i}}{a\,\sin(\theta_{1i} - \theta_{2i})\,\sin\theta_{3i}}$$
$$J_{3i} = -\frac{\sin\theta_{2i}}{a\,\sin(\theta_{1i} - \theta_{2i})}.$$

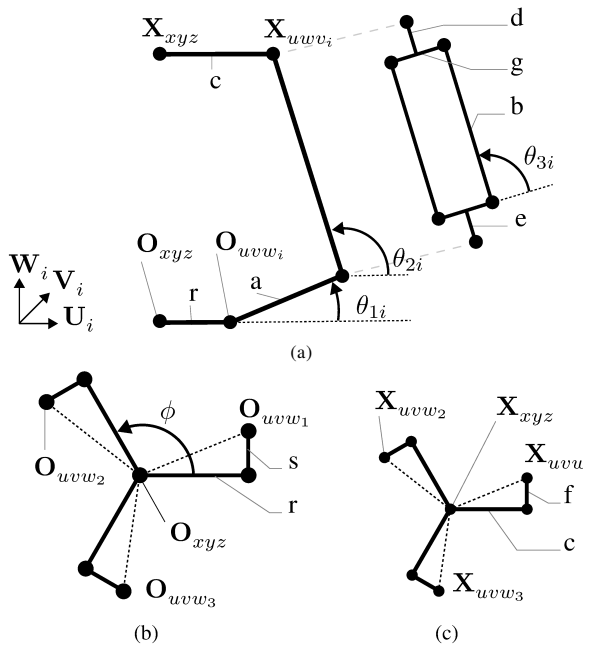

Fig. 2. Fig (a) shows the schematic of the i^{th} leg in the u_i, v_i, w_i reference frame. The leg attaches to the base at $\mathbf{O}_{uvw_i}$, shown in (b), and to the top platform at $\mathbf{X}_{uvw_i}$, shown in (c)

TABLE I. Links (top row) of the haptic device and their corresponding lengths in millimetres (bottom row).

Link Lengths in millimetres								
a	b	c	d	e	f	g	r	s
60.0	102.5	14.4	13.0	13.0	25.0	27.9	36.6	27.2

C. Forward Kinematics

In contrast to the inverse kinematics, the forward kinematics of a parallel manipulator is significantly more difficult to compute as it involves solving a 32nd order polynomial with a total of 32 solutions, of which 16 are extraneous [30], [31]. The high computational cost, the considerable difficulty of implementation, and the multitude of solutions make the analytical solution impractical to use. As a result, the forward kinematics of parallel manipulators is commonly approximated using iterative solvers like the damped Newton's method [33], [34].

Similar to other variants of iterative solvers, damped Newton's Method starts with an initial position guess and then iteratively improve the solution until the error is minimized. The method gives the position of the end-effector at iteration k

$$\mathbf{X}_k = \mathbf{X}_{k-1} - \mathbf{J}(\boldsymbol{\theta}_{k-1})^{\mathrm{T}}\,(\boldsymbol{\theta} - \boldsymbol{\theta}_{k-1})\,G \tag{8}$$

where $\mathbf{X}_{k-1}$ is the estimated position taken at sample $k-1$ that is used to find the joint angles $\boldsymbol{\theta}_{k-1}$ and the Jacobian matrix $\mathbf{J}(\theta_{k-1})^{\mathrm{T}}$. The actual angular position of θ_{1i} is represented by $\boldsymbol{\theta}$, and G is an adaptive scaling factor. The error between the estimated and actual position is $E(k) = ||\boldsymbol{\theta} - \boldsymbol{\theta}_{k-1}||$. If the error between iterations decreased, $E(k) < E(k-1)$, then the solution is accepted, $\mathbf{X}_{k+1} = \mathbf{X}_k$, and the loop is repeated. If, however, the error increased, $E(k) > E(k-1)$, the solution

is rejected, $\mathbf{X}_k = \mathbf{X}_{k-1}$, and the scaling factor is decreased $G = G/2$. The loop ends after a set number of iterations, or when an acceptable answer is reached. In most cases, the solver converges onto a solution within 15 iterations [35].

Once the angle of all joints are calculated, the Jacobian matrix can be calculated using (7). Using the Jacobian it is also possible to convert forces into joint torques of the device. For a passive haptic device, however, the torque generated by the brakes depends on factors other than the desired torque.

III. Modelling the Force Output of a Passive Haptic Device

The kinematic structure of the device creates a non-linear relationship between the motion and forces at the end-effector and at the brakes. The description of the force output of a passive device is further complicated by the nonlinear force output capability of the device. As a result, the analysis of passive devices is typically conducted using reference forces [36].

A. Reference Forces

The inverse transpose of the Jacobian matrix relates the torque of all joints to the force at the end-effector [37],

$$\mathbf{F} = \left(\mathbf{J}^{-1}\right)^{\mathrm{T}} \boldsymbol{\tau} \tag{9}$$

where the torque applied by each actuator is,

$$\boldsymbol{\tau} = \begin{bmatrix}\tau_1 & \tau_2 & \cdots & \tau_n\end{bmatrix}^{\mathrm{T}}.$$

Let us examine the 2-DOF manipulator shown in Fig. 3(a). Applying an input $\tau_2 = 1\,\mathrm{N}\cdot\mathrm{m}$ and $\tau_1 = 0\,\mathrm{N}\cdot\mathrm{m}$ generates the force output represented by $+\mathbf{R}_2$. It follows that $+\mathbf{R}_2$ corresponds to the second column of the inverse transpose Jacobian,

$$(\mathbf{J}^{\mathrm{T}})^{-1} = \begin{bmatrix} R_{x_1} & R_{x_2} & \cdots & R_{x_i} \\ R_{y_1} & R_{y_2} & & R_{y_i} \\ \vdots & & \ddots & \vdots \\ \underbrace{R_{\gamma_1}}_{\mathbf{R}_1} & \underbrace{R_{\gamma_2}}_{\mathbf{R}_2} & \cdots & \underbrace{R_{\gamma_i}}_{\mathbf{R}_n} \end{bmatrix}. \tag{10}$$

By extension, the i^{th} column in the inverse transpose of the Jacobian $\mathbf{R}_i$ represents the *reference force* generated by actuator i. These reference forces give a more intuitive understanding of the relationship between the torque applied at a joint and the resulting forces at the end-effector. This paradigm, introduced in [38] and refined in [16], [39], helps in understanding and describing the output force of any haptic device. This is the focus of the following section.

B. Force Output of a Haptic Device

An ideal haptic device can create any force output. This can be represented as a sum of the scaled reference forces from (10),

$$\mathbf{F}_a = \sum_{i=1}^{n} a_i\,\mathbf{R}_i \tag{11}$$

where $a_i \in \mathbb{R}$ represents the scaling factors of the reference force i. In Fig. 3(a) we can generate forces $+\mathbf{R}_1$ and $+\mathbf{R}_2$. To generate $\mathbf{F}_1$, however, $-\mathbf{R}_1$ and $+\mathbf{R}_2$ must be used. By setting a_i to a negative value, the direction of the resulting force will equal $-\mathbf{R}_i$. On the other hand, to generate $+\mathbf{R}_i$, no sign change is necessary, meaning $a_i > 0$. Note that (9) and (11) are equivalent, thus making $a_i = \tau_i$.

For an ideal device, there always exists a set of a_i values that can make the output force $\mathbf{F}_a$ and the desired force $\mathbf{F}_d$ equal to each-other, $\mathbf{F}_a = \mathbf{F}_d$. For a realistic device, however, there is a limit to the torque an actuator can generate, thus, the scaling factor must be bound to $a_i \in \mathbb{R}[-\tau_{max_i} \quad \tau_{max_i}]$, where τ_{max_i} is the maximum torque output of the i^{th} actuator. This confines the force range of the device and leads to the limited manipulability shown as the region Ω_1 in Fig. 3(b). The contour of this region represents the manipulability of a device in a given direction. A realistic device, therefore, can create a finite force output in all directions but the magnitude of the maximum force in any of these directions can vary.

C. Force Output of a Passive Device

When a haptic device uses brakes as actuators, the force output is further constrained. Recall that when moving, a brake can only generate torque opposing the angular velocity of the respective joint, i.e. $\dot{\theta}_i\,\tau_i < 0$. As a result, we can control the magnitude of the force generated at the end-effector but not its direction. If a brake is stationary, however, neither the direction nor the magnitude of the torque can be controlled. Instead, the brake generates torque opposing any torque input τ_{in}, i.e. $\tau_{out} = -\tau_{in}$. Consider the case with two moving brakes in Fig. 3(a), where joint 1 rotates in the positive (CW) direction and joint 2 rotates in the negative (CCW) direction. As a result, the device can produce a negative torque at joint 1 and a positive torque at joint 2. At the end-effector the torque developed in joint 1 creates the reference force $-\mathbf{R}_1$, and the torque in joint 2 gives $+\mathbf{R}_2$.

To describe the force output of a passive device, (11) must be modified to account for these additional restrictions. The sign of the scaling factors is determined by the velocity or torque input to each brake. For a positive velocity, the brake can only generate a negative torque, which results in a negative reference force, and vice-versa. If the velocity is zero the sign is determined by the force input to the device. The force output in such a case must oppose the force input, i.e. $\mathbf{F}_d \cdot \mathbf{F}_{in} < 0$. This condition must be evaluated for each actuator, which means that both the desired and the input forces must be projected onto the relevant reference force. If the product of the two projections is less than zero, i.e., $(\mathbf{R}_i \cdot \mathbf{F}_{in})(\mathbf{R}_i \cdot \mathbf{F}_d) < 0$, the forces oppose each other and the reference force can be used to display the force, otherwise the brake must be released. Thus, the sign of the scaling factor in a passive device is determined by

$$S(\dot{\theta}_i) = \begin{cases} -1 & \text{if } \dot{\theta} > 0 \\ H\left[-(\mathbf{F}_{in} \cdot \mathbf{F}_d)(\mathbf{R}_i \cdot \mathbf{F}_d)\right] \frac{\mathbf{F}_{in} \cdot \mathbf{R}_i}{||\mathbf{R}_i||^2\,\alpha_i} & \text{if } \dot{\theta} = 0 \\ 1 & \text{if } \dot{\theta} < 0 \end{cases} \tag{12}$$

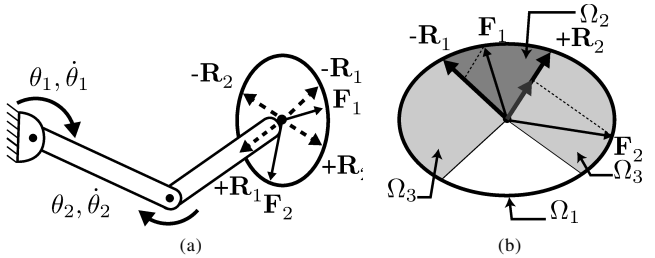

Fig. 3. (a) A 2-DOF manipulator and its reference force vectors. (b) Regions formed by the reference forces of the device in (a), and the decomposition of the forces along the reference vectors.

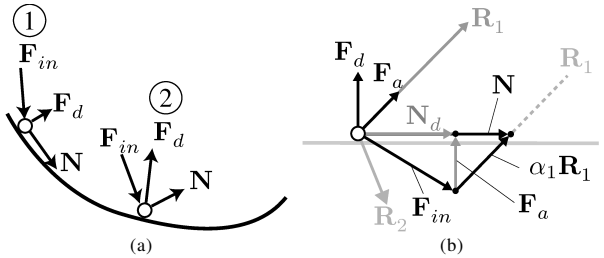

Fig. 4. (a) Ideal and realistic forces acting at an end-effector of a haptic device when rendering a frictionless surface. (b) Sliding can be maintained even if the force output cannot be accurately displayed.

which yields either -1, the force applied by a stationary brake divided by α_i, or 1, and where $H()$ is the Heaviside step function which determines if a force is displayable[1].

Since the direction of the scaling factor is determined by (12), we must redefine the scaling factor such that its value is always positive. To differentiate between the active and passive devices, let us use $\alpha_i \in \mathbb{R}\,[0 \quad \tau_{max}]$ when referring to passive devices. Now, the range of forces a passive device can generate is given by

$$\mathbf{F}_a = \sum_{i=1}^{n} \alpha_i \, S(\dot{\theta}_i) \, \mathbf{R}_i. \tag{13}$$

Note, that in a static case α_i is eliminated from the equation.

Unlike in (11), the device can only generate a desired force provided that a solution to (13) exists such that $\mathbf{F}_a = \mathbf{F}_d$. As shown in Fig. 3(b), this greatly restricts the range of *displayable forces*, i.e, the forces such a device can generate. The force output of the passive device is bounded by Ω_2 where $\Omega_2 \subset \Omega_1$. Such a limited range of force makes it difficult to implement passive devices in most applications. The next section describes a method of expanding this range by approximating the desired forces.

D. Force Displayability of a Passive Device

In Fig. 3, the force $\mathbf{F}_2$ cannot be displayed by the device since +$\mathbf{R}_1$ is required to replicate the force but only -$\mathbf{R}_1$ is available. It is still possible to use a component of +$\mathbf{R}_2$ to approximate $\mathbf{F}_2$. This is shown in Fig. 3(b) where $\mathbf{F}_2$ is projected onto +$\mathbf{R}_2$, as indicated by the dotted line. This projection represents the closest approximation of $\mathbf{F}_2$ that +$\mathbf{R}_2$ can generate alone. As long as this projection is greater than zero, the reference force may be used. In Fig. 3(b), the forces satisfying this condition are bounded by Ω_3, where $\Omega_3 \subset \Omega_1$. Notice that $\Omega_2 \subset \Omega_3$ which means that if a force can be reproduced based on (13) it can also be approximated. Thus, the best approximation of the desired force becomes:

$$\mathbf{F}_a = \sum_{i=1}^{n} \alpha_i \, D_i \, \mathbf{R}_i \tag{14}$$

where $\mathbf{F}_a \simeq \mathbf{F}_d$, and

$$D_i = S(\dot{\theta}_i) \, H\left(S(\dot{\theta}_i) \, \mathbf{R}_i \cdot \mathbf{F}_d\right). \tag{15}$$

[1]The force applied by a stationary brake is uncontrollable, therefore the term α_i needs to be eliminated in the formulation. Dividing the result of (12) by α_i is the simplest method of achieving this mathematically.

It may be convenient to think of (14) as a matrix, such as,

$$\mathbf{F}_a = \begin{bmatrix} \mathbf{R}_1 & \mathbf{R}_2 & \cdots & \mathbf{R}_i \end{bmatrix} \, (\boldsymbol{\alpha} \circ \mathbf{D}) \tag{16}$$

where $\boldsymbol{\alpha} = \begin{bmatrix} \alpha_1 \; \alpha_2 \; \cdots \; \alpha_i \end{bmatrix}^T$, $\mathbf{D} = \begin{bmatrix} D_1 \; D_2 \; \cdots \; D_i \end{bmatrix}^T$, and the operator $\circ$ is the Hadamard product. If $\mathbf{F}_a$ has a full rank, the force can be displayed accurately. If the rank is not full but also not zero, the force output of the device may be approximated. If the rank is zero no forces can be displayed. Let us explore a method of approximating the desired force using 1, 2, or 3 reference forces.

IV. Controller Design

The control approach chosen here forces the device to slide along a rigid frictionless surface. The sliding motion reduces brake stiction and force distortions induced by force approximation. The sliding is enforced by balancing the forces at the end-effector such that they are in an equilibrium along the direction normal to the surface.

Consider a virtual environment composed of a wall defined by an arbitrary surface, with some stiffness and no friction, like the one in Fig. 4(a). In an ideal case shown in Fig. 4(a) ①, the user applies force $\mathbf{F}_{in}$ to the device which, in turn, generates a force output $\mathbf{F}_a = \mathbf{F}_d$. The sum of these two forces result in a net force

$$\mathbf{N} = \mathbf{F}_a + \mathbf{F}_{in} \tag{17}$$

which acts parallel to the surface of the plane. This means that the user is not allowed to penetrate the surface while moving along the surface. Thus, in an ideal situation the net force $\mathbf{N}$ should act tangentially to surface i.e, the normal component of $\mathbf{N}$ is

$$||\mathbf{N}^{\perp}|| = 0 \tag{18}$$

which will be referred to as the *sliding constraint*. Note that there always exists a theoretical solution to the sliding constraint, however due to physical limitations of the haptic device it may not be possible to adequately render the force required to satisfy the constraint.

In reality, haptic devices struggle to satisfy this condition primarily due to delays [14]. As a result, the force applied by the device can be too high, pushing the user out of the virtual wall, like in Fig. 4(a) case ②. Because the brake only dissipates energy, applying an excessive force blocks the user from moving, resulting in stiction [29], [39]. By inducting the sliding on the surface, the user is free to move at least in one

direction unimpeded, reducing the likelihood of stiction and preserving the geometry of the virtual object.

However, completely eliminating the normal component of the net force creates problems. Consider a situation where the end-effector of a passive device penetrates a virtual surface. Eliminating the normal component of the force means that the device cannot push the user out of the wall, which could minimize the surface penetration. By allowing the net force to have a small positive component perpendicular to the plane, the device will slowly move out of the wall. To control this behaviour, let $||\mathbf{N}^{\perp}|| = c$ where $c \in \mathbb{R}^{+}_{\rightarrow 0}$ is the net force constant. If a positive component of the net force is desired, c should be set to a small positive value. On the other hand, if no net force is to be displayed set $c = 0$.

To eliminate stiction in a passive device the sliding constraint must be satisfied. Note that there are many possible forces that could satisfy this constraint. If the desired force cannot be displayed by the device, it is possible to generate an approximate force to satisfy the sliding constraint.

A. Force Approximation using 1 Reference Force

Consider the situation depicted in Fig. 4(b). Like in Fig. 4(a), the frictionless virtual wall creates $\mathbf{F}_d$ normal to the surface of the wall, to stop the user from penetrating the wall. Since $\mathbf{F}_d$ does not lie on either one of the reference forces, both $\mathbf{R}_1$ and $\mathbf{R}_2$ will need to be used. Notice that the projection of $\mathbf{R}_2$ onto $\mathbf{F}_d$ is negative meaning that it must be approximated with only one force, $\mathbf{R}_1$. Let us now consider how such a force can be used to approximate $\mathbf{F}_d$.

Using only one actuator, the direction of the force output will always be the same. What changes is the net force acting on the end-effector of the device. Notice that in Fig. 4(b) the ideal net force $\mathbf{N}_d$, i.e. the sum of force input and the desired force, acts parallel to the wall. By applying some scaling factor α_1 to $\mathbf{R}_1$, the net force on the end-effector $\mathbf{N}$ will be generated. The direction of both $\mathbf{N}_d$ and $\mathbf{N}$ will be parallel to the wall but their magnitude will differ. This means that in either case the user will be unable to penetrate the virtual wall and in the approximated case interaction with the wall will cause more sliding. As shown in [39], to find the value of α_1 that satisfies the sliding constraint, let us take the sum of forces along the direction perpendicular to the surface of the wall,

$$||\mathbf{N}^{\perp}|| = \mathbf{F}_{in} \cdot \mathbf{F}_d + \alpha_i \, (\mathbf{R}_i \cdot \mathbf{F}_d) \tag{19}$$

and solve for α, replacing $||\mathbf{N}^{\perp}||$ with the net force constant

$$\alpha_i = \frac{c - \mathbf{F}_{in} \cdot \mathbf{F}_d}{\mathbf{R}_i \cdot \mathbf{F}_d}. \tag{20}$$

When only one reference force is available to approximate a desired force there is at most only one solution that satisfies the passivity constraint. However, as discussed in [36] in devices with more DOF the forces may be approximated using several reference forces at once. For instance in a 3-DOF device, a force can be approximated using two reference forces. Using two reference forces allows the controller to better control the direction of sliding, thus, improving the force output sensation.

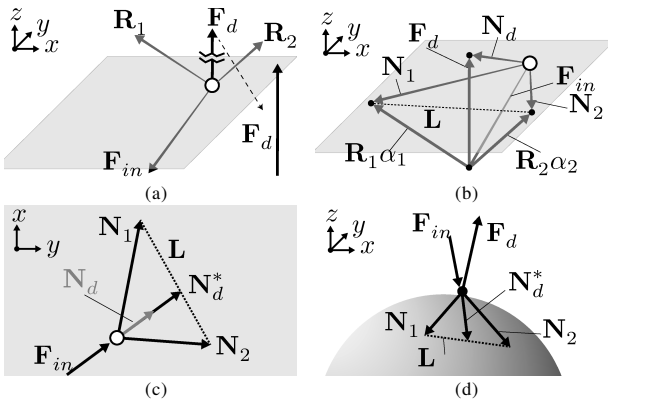

Fig. 5. (a) Two reference vectors can approximate a force resulting from touching a plane. (b) Either of the reference forces can create a force satisfying sliding constraint. In (c) a range of net forces produced by the device is shown. By choosing a net force with the same direction as the projection of $\mathbf{N}_d$ onto the plane, results in sliding motion approximating the rendered geometry, as shown in (d).

B. Approximating Forces with 2 Reference Forces

Consider, the case shown in Fig. 5(a) with a desired force $\mathbf{F}_d$, a force input $\mathbf{F}_{in}$, and two displayable reference forces $\mathbf{R}_1$ and $\mathbf{R}_2$. According to (20) each force can independently generate a net force satisfying the sliding constraint

$$\mathbf{N}_i = \mathbf{F}_{in} + \mathbf{R}_i \, \alpha_i \tag{21}$$

as shown in Fig. 5(b). Both $\mathbf{N}_1$ and $\mathbf{N}_2$ satisfy the sliding constraint, though their directions vary significantly. Both of these net forces lie on a plane with a normal unit vector

$$\mathbf{P} = \frac{\mathbf{N}_1 \times \mathbf{N}_2}{||\mathbf{N}_1||\mathbf{N}_2||}, \tag{22}$$

containing all possible forces satisfying the sliding constraint[2].

The forces a device can generate are all positive combinations of $\mathbf{R}_1$ and $\mathbf{R}_2$. These forces lie on a plane containing these two vectors. The intersection of the plane containing these forces with the plane satisfying the sliding constraint forms a line

$$\mathbf{L}_r = \mathbf{N}_1 + \mathbf{L} \, b \tag{23}$$

where $b \in \mathbb{R} \; [0 \quad 1]$ is a controllable parameter, and

$$\mathbf{L} = \mathbf{R}_1 \, \alpha_1 - \mathbf{R}_2 \, \alpha_2 = \mathbf{N}_1 - \mathbf{N}_2. \tag{24}$$

Any point on this line can be generated using the two reference vectors and, because the lines lie on the plane defined by $\mathbf{P}$, satisfies the sliding constraint. Clearly, b can have infinitely many solutions. Which solution results in the most accurate rendering of the virtual surface?

Assume we want to render a 3D object, like a sphere, with a 3-DOF device that can only approximate the desired force with two actuators. The net forces resulting from this interaction can be seen in Fig. 5(d), along with the resulting line $\mathbf{L}_r$. Applying $\mathbf{R}_1$, however, results in $\mathbf{N}_1$ which is tilted counterclockwise from $\mathbf{F}_{in}$. Similarly, by using $\mathbf{R}_2$ the resulting net force $\mathbf{N}_2$

[2]If α_i was calculated with $c = 0$ then $\mathbf{P} \parallel \mathbf{F}_d$. On the other hand, if $c > 0$, $\mathbf{P}$ will act at an angle from $\mathbf{F}_d$.

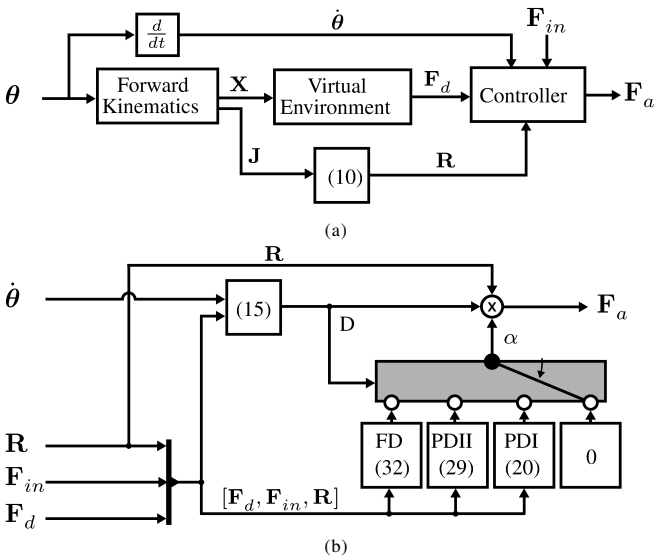

Fig. 6. (a) The general structure of the proposed controler. (b) A detailed breakdown of the controller, and various control cases: FD - Fully displayable, PDII - Partially displayable using two actuators, PDI - Partially displayable using one actuator, and 0 for non-displayable forces.

is tilted clockwise from the user input. From Fig. 5(d), the desired net force,

$$\mathbf{N}_d = \mathbf{F}_{in} + \mathbf{F}_d \tag{25}$$

lies between the two reference vectors and its scaled copy $\mathbf{F}_d^*$ lies on $\mathbf{L}_r$, making it displayable. The controller seeks to find the values of α_i that will result in $\mathbf{F}_a = \mathbf{N}_d^*$. In reality the desired force does not necessarily satisfy the sliding constraint as is the case in Fig. 5(a). We must, therefore, start by projecting $\mathbf{N}_d$ onto the plane defined by $\mathbf{P}$

$$\mathbf{N}_d' = \frac{\mathbf{P}}{||\mathbf{P}||^2} \times (\mathbf{N}_d \times \mathbf{P}). \tag{26}$$

It is unlikely that this projection will coincide with the achievable net forces represented by $\mathbf{L}_r$. If $\mathbf{N}_d$ is scaled to intersect with $\mathbf{L}_r$ the resulting net force will be displayable. To find this intersection point $\mathbf{N}_d^*$, an augmented matrix may be used such that[3],

$$\begin{bmatrix} \mathbf{L} & \mathbf{N}_1 \mid \mathbf{N}_d' \end{bmatrix} = \left[\begin{array}{cc|c} 1 & 0 & b_1 \\ 0 & 1 & b_2 \\ 0 & 0 & 0 \end{array}\right] \tag{27}$$

which when solved yields two constants; b_2 can be disregarded, while $b_1 \in \mathbb{R}$ $\begin{bmatrix} 0 & 1 \end{bmatrix}$ gives the location of the intersection point

$$\mathbf{N}_d^* = \mathbf{N}_1 + \mathbf{L}\, b_1. \tag{28}$$

Finally, knowing the desired location, the set of α_i that will create the desired force is found using[4]

$$\begin{bmatrix} \mathbf{R}_1 & \mathbf{R}_2 \mid \mathbf{N}_d^* \end{bmatrix} = \left[\begin{array}{cc|c} 1 & 0 & \alpha_1 \\ 0 & 1 & \alpha_2 \\ 0 & 0 & 0 \end{array}\right]. \tag{29}$$

[3]The augmented matrix equates the equation of $\mathbf{L}_r$ and $\mathbf{N}_d'$. Note that $\mathbf{L}_r$ contains two vectors, the starting point $\mathbf{N}_1$ and the direction $\mathbf{L}$, while $\mathbf{N}_d'$ starts at the origin eliminating the need for the starting point

[4]Both (27) and (29) are 3x3 matrices with a row of zeros. This indicates that the combined vectors act in a single plane.

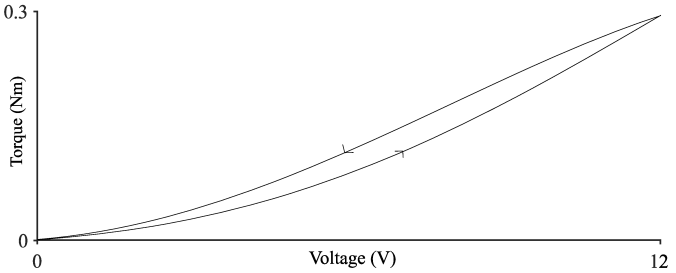

Fig. 7. Hysteresis curve for Placid Industries B-2 Particle Brake [40]

It may be possible for b_2 to exceed its bounds. In such a case the nearest reference force should be used as the approximation. If $b_2 < 0,\ \mathbf{F}_a = \mathbf{R}_1\, \alpha_1$, and if $b_2 > 1,\ \mathbf{F}_a = \mathbf{R}_2\, \alpha_2$.

C. Approximating Forces with 3 Reference Forces

A fully displayable force may at times violate the sliding constraint due to discretization, delays, etc. Applying such a force directly can result in stiction. As a result, it is better to modify the force output such that $\mathbf{N}^{\perp} \simeq 0$. Like in previous cases, we can find a value of α_i to satisfy the sliding constraint. Unlike in previous cases, the calculation of the scaling factors α_i can be simplified by applying a different scaling factor β directly to the desired torque

$$\alpha_i = \tau_{d_i}\, \beta \tag{30}$$

where β is the scaling factor, and τ_{d_i} is calculated using (9). To find β, once again, the sum of forces perpendicular to the plane is set to c,

$$\mathbf{N}^{\perp} = c\, \frac{\mathbf{F}_d}{||\mathbf{F}_d||} = \mathbf{F}_d \frac{\mathbf{F}_{in} \cdot \mathbf{F}_d}{||\mathbf{F}_d||^2} + \beta\, \mathbf{F}_d \tag{31}$$

and then solved for β

$$\beta = \frac{c}{||\mathbf{F}_d||} - \frac{\mathbf{F}_d \cdot \mathbf{F}_{in}}{||\mathbf{F}_d||^2}. \tag{32}$$

Applying β to the desired torques simply scales the magnitude of the force satisfying the sliding constraint.

D. Controller Design Summary

Two inputs are required to control the haptic device, namely the angular position of each actuator and the user force input, as shown in Fig. 6(a). The position of the end-effector, found using the forward kinematics, is then used in the virtual environment to calculate the desired force. The controller uses the desired force, along with the reference force and angular velocity, to determine the force output of the device.

The controller attempts to satisfy the sliding constraint reducing the effects of stiction and improving the force output capability of the device, using the method outlined in Fig. 6(b). First, the number of actuators capable of approximating the force is found using (15). Based on their number, the force is approximated using 1, 2 or all 3 actuators where each method is outlined in Section IV-A, IV-B, and IV-C respectively.

V. Experimental Evaluation

Frictionless objects are the most difficult objects to render using a passive haptic device, making them a good evaluation benchmark. A device capable of rendering a smooth virtual surface will also be able to render other types of environments with ease. To evaluate this controller six surfaces were used: 4 unique inclined planes identified by the angle separating them form the horizontal plane, shown in Fig. 8(a), a convex, and a concave surface, shown in Fig. 9. These surfaces were selected to either isolate a single mode of operation or test a combination of them.

Scenario 1 - $10°$ plane: The nearly horizontal plane can be rendered using all 3 actuators.

Scenario 2 - $30°$ plane: When rendering this plane, the device will be able to use two actuators for the majority of the trial, testing the two reference force approximation method.

Scenario 3 - $45°$ plane: This plane is oriented such that the device can approximate the force using only one actuator, hence testing the single reference force approximation method.

Scenario 4 - $45°$ plane: To render this plane the device has to switch between one and two reference force approximation methods, testing the controller's ability to switch between the different control modes.

Scenario 5 - Convex surface: To generate this geometry the desired force varies from vertical to horizontal. Therefore this test evaluates all aspects of the controller, starting with displayable forces and finishing with approximations.

Scenario 6 - Concave surface: This surface is opposite of the one in Scenario 5. Initially the desired forces must be approximated, and at the end, the forces are fully displayable.

Each of these scenarios was run with the net force constant values set to $c = 0$, $c = 0.1$, and $c = 0.5$. To generate these geometries we developed a virtual environment which simulated interactions of the device with the virtual surfaces.

A. Virtual Environment

The desired force resulting from contact with a virtual frictionless object is dependent only on the depth of object penetration. As a result, the desired force for all cases is

$$\mathbf{F}_d = \begin{cases} \hat{\mathbf{u}}\, d\, k & \text{if } d < 0 \\ 0 & \text{otherwise} \end{cases} \tag{33}$$

where $\hat{\mathbf{u}}$ is the unit vector normal to the surface, d is the penetration depth into the wall, and k is the stiffness of the plane. The surfaces used in the experiments had stiffness $k = 75\,\mathrm{kN/m}$. The unit vector normal to the inclined planes $\hat{\mathbf{u}}_p$ is known and it can be used to determine the penetration depth,

$$d = d_p = \hat{\mathbf{u}}_p \cdot (\mathbf{X} - \mathbf{X}_f) \tag{34}$$

where $\mathbf{X}$ is the position of the end-effector, and $\mathbf{X}_f$ is the vertical offset of the plane from the workspace origin.

A convex surface, on the other hand, is defined by the radius r from a focal point $\mathbf{O}$. Using this point and the position of the end-effector, the penetration depth and the normal unit vector for this surface are, respectively:

$$d = d_{vex} = ||\mathbf{O} - \mathbf{X}|| - r \tag{35}$$

$$\hat{\mathbf{u}} = \hat{\mathbf{u}}_{vex} = \frac{\mathbf{O} - \mathbf{X}}{||\mathbf{O} - \mathbf{X}||} \tag{36}$$

while for a concave surface the direction of the two is inverted, $d_{con} = -d_{vex}$ and $\hat{\mathbf{u}}_{con} = -\hat{\mathbf{u}}_{vex}$.

B. Experimental Setup

A Humusoft MF 634 Data Acquisition Card measured the angular position from the encoders and controlled the voltage applied to the brakes. The forward kinematics, the virtual environment, and the controller were programmed using Simulink 2019a. The simulation ran at 2 kHz in the external mode, which eliminated delays in the execution of the code.

The torque of the brake was controlled using a PWM signal with frequency of 35 kHz. The relationship between duty cycle (i.e. voltage) and the torque of the brake, shown in Fig. 7, indicates that the brakes are non-linear, and subject to hysteresis. In these experiments, however, the hysteresis was neglected, and only the increasing curve in Fig. 7 was used.

To ensure consistent behaviour of the device, a 500 g mass was placed at the end-effector generating a constant downward force of 4.90 N. It was assumed that the mass of the device observed from the end-effector was 350 g meaning that the total force acting on the end-effector was 8.3 N. Notably, a force sensor was not used in these experiments. During each trial, the end-effector was lifted using a string to a region outside of the virtual object, and then slowly released onto the virtual surface.

C. Results

The experimental results are divided into two sets: Fig. 8 shows the results for the four inclined planes while the results for the two curved surfaces are in Fig. 9. The figures are divided into sets for each evaluated scenarios. Each set contains 3 runs each with a different value of the net force constant. The first figure in each set, labelled (a), contains a 3-D plot of the rendered surface along with the path taken by the end-effector when it was in contact with this surface. Next, figures labelled (b) show the projected path of the end-effector onto the surface it slid on. The depth of plane penetration for all cases is shown in (c) while (d) shows the number of actuators used to display the forces. The magnitude of the applied force is plotted in (e), while the estimated component of the force acting perpendicular to the plane is shown in (f).

VI. Discussion

To asses the effectiveness of the controller, let us consider the controller's ability to prevent stiction, the depth of surface penetration, and the effects of the net force constant.

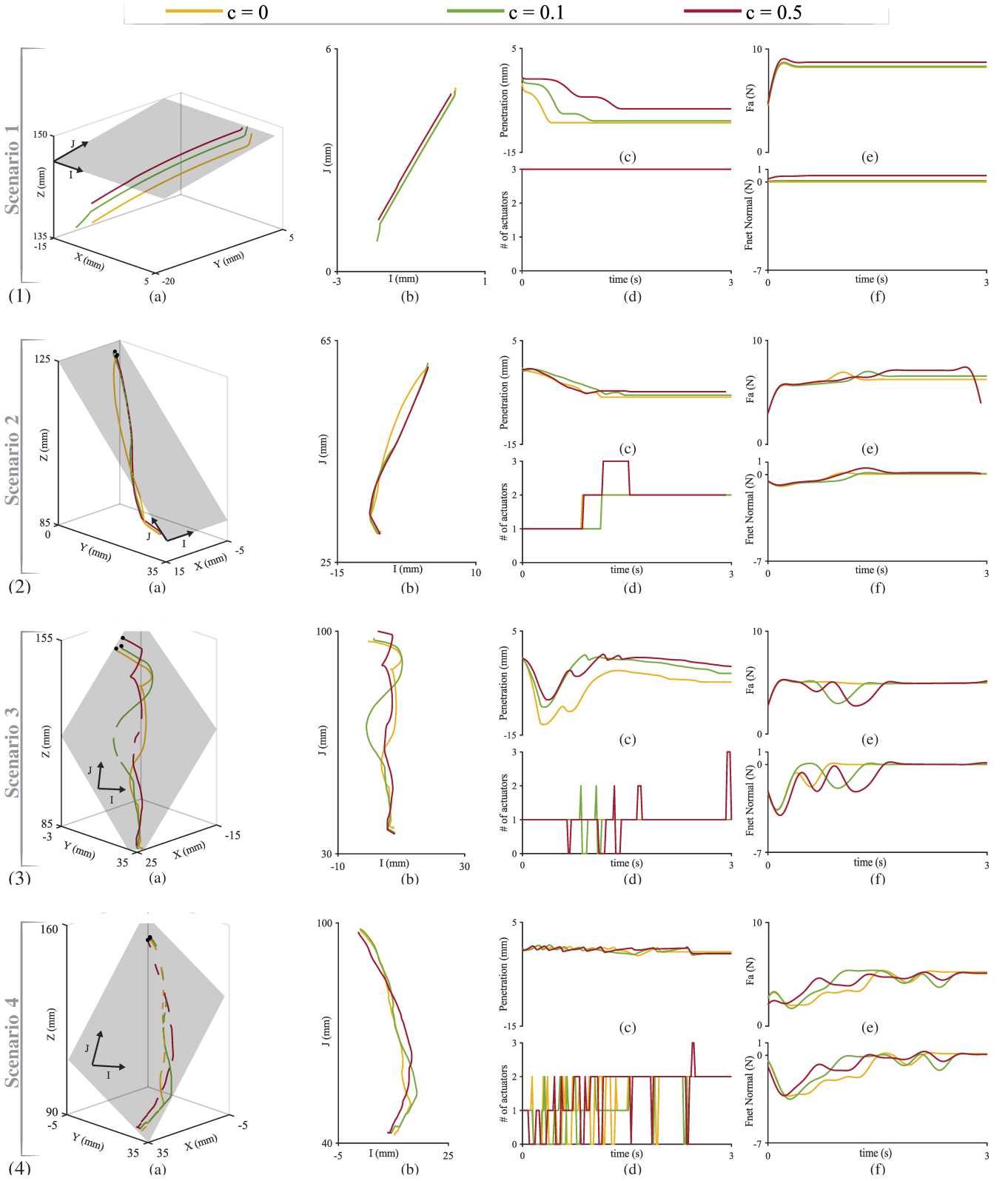

Fig. 8. The results of rendering four inclined planes: a 10° in (1) , 30° in (2), 45° in (3), and 45° (4). For each case, the 3D overview of device's path along with the rendered geometry is shown in (a). In (b) the projection of the path onto the virtual plane is shown in the coordinate system of the plane. (c) shows the depth of penetration, while (d) displays the number of actuators used to generate the force. The filtered magnitude of the applied force is shown in (e), while the filtered net force perpendicular to the plane is shown in (f).

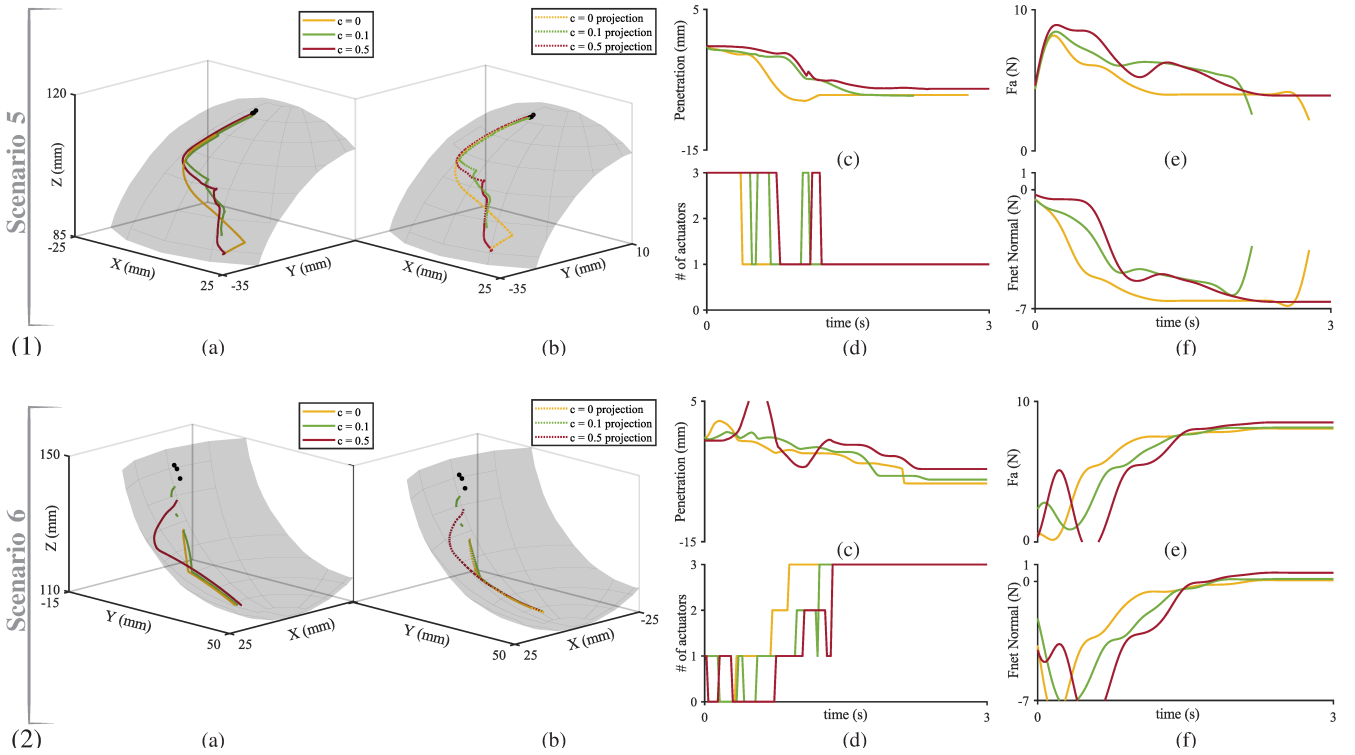

Fig. 9. The results of rendering two curved surfaces: one convex (1), and the other concave (2). For each case, the 3D overview of device's path along with the render surface is shown in (a). (b) shows the projection of the path onto the surface. (c) shows the depth of penetration, while (d) displays the number of actuators used to generate the force. The filtered magnitude of the applied force is shown in (e), while the filtered net force perpendicular to the surface is shown in (f).

A. Stiction and Sliding Along a Plane

In an ideal situation, after initiating the contact with the surface the end-effector moves smoothly along the surface. To observe the motion of the end-effector with respect to the virtual surface we project the path of the device onto the surface in Fig. 8(c) and Fig. 9(c). The projection of the path on an inclined plane should be a vertical line, indicating that the device moved down the plane without any sideways motion. For a curved surface, the equivalent of the ideal path is a longitudinal line.

To set a baseline for evaluation, we attempted to render required geometries without using our control scheme by actuating the brakes with the desired torque. In all cases, this lead to immediate stiction as the desired force imminently saturated the brakes. The results for this case were indistinguishable among different test scenarios. The end-effector did not move past the initial contact point with the plane, and due to saturation, the same force was applied for all the case. This behaviour was consistent through all the experiments, and thus, it is not shown here. In contrast, when using the controller the device consistently slid along the surfaces, as shown in Fig. 8-(b) for scenarios 1 to 4 and in Fig. 9-(b) for scenarios 1 and 2.

In the majority of the tests, however, the projection of the line was not perfectly vertical which indicates that the device moved sideways on the plane. One of the reasons for this motion is the effect of the single reference force approximation, like in Fig. 8 for scenario 3 and in Fig. 9 for scenario 1. When only one reference force was available, as expected, the direction of sliding was not controllable. In all other runs, the sideways motion was consistent between runs. This may have been caused by the initial conditions like the horizontal velocity of the end-effector and its initial contact point with the plane. The maximum sideways motion was approximately 10 mm and it occurred in scenario 4, shown in Fig. 8. This error may be eliminated in cases where two or more actuators are used, and by obtaining a more accurate force input which would account for the force resulting from the dynamics of the device. Despite this error the controller eliminates stiction and induce sliding along the various surfaces.

B. Surface Penetration

Ideally, the device should stop the user from penetrating the rendered surfaces. Any plane penetration is a result of an imbalance of forces perpendicular the virtual surface. When rendering the 10° plane, shown in Fig. 8 for scenario 1, the balance of forces was theoretically maintained at or near 0, depending on the value of the net force constant, as shown in (f). In (c), however, the surface penetration clearly increased during the run, and ultimately levelled near the depth of 10 mm. The difference between the theoretical and the actual behaviour suggests that the cause of this penetration is external to the controller. Likely, this error is caused by a combination of the delay in the response time of the brakes, the simplified

model of the device dynamics, and error in approximating the hysteresis of the brakes.

Surface penetration was also caused by the single brake force approximation. Consider the net force perpendicular to the plane in Fig. 8 for scenarios 2 to 4 and in Fig. 9 for scenarios 1 and 2. In these cases, the net force was less than zero at some instances which indicates that the controller could not eliminate the non-zero net force. Notice, also, that these cases correspond to instances when a single reference force approximation was in use and thus the force output capability of the device is bounded to the force and torque capability of a single actuator.

The plane penetration is, therefore, the result of unmodelled behaviours, linearization, and the single reference force approximation. Improving the model can result in a significantly smaller penetration depth in all of the runs. Despite these limitations and simplifications, the controller was able to stop the user from penetrating the virtual surfaces. By tuning the net force constant, the effects of plane penetration can be improved even without the aforementioned improvements.

C. Tuning the net force constant

The net force constant c from (20) is a tunable parameter which changes the balance of forces perpendicular to the surface. If $c = 0$, the device will move without attempting to eliminate any potential surface penetration. Increasing the value of the net force constant increases the magnitude of the applied force, as shown in Fig. 8(e) and Fig. 9(e). This, in turn, results in a higher net force acting perpendicular to the plane, as shown in Fig. 8(f) and Fig. 9(f). The effect of c on both the applied and the net force is the easiest to observe in Fig. 8 for scenario 1 since all the forces in this scenario are fully displayable.

By increasing the net force perpendicular to the plane, the device can eventually eliminate penetration, as shown in Fig. 8 for scenario 3. In some cases, however, an increase in the net force constant caused the device to move out of the surface repeatedly, leading to the chattering visible in Fig. 8 for scenario 4. To eliminate it, the net force constant needs to be reduced, which should result in a plane that feels smooth.

D. Rendering Other Virtual Environments

The testing scenarios considered here represent the worst-case scenario for a passive haptic device; simple frictionless objects with constant force input. In most haptic applications, however, the virtual environment behaves much differently from these extreme cases. For instance, sliding along a plane is an uncommon occurrence. It is much more common for the device to interact with soft objects, such as human tissue, which involves rendering damping and friction. Forces due to friction oppose the motion of the user, and the resulting desired force should, therefore, be easier to recreate. Virtual environments are often significantly more complex than spheres and planes used in the validation experiments. If the rendered object is more intricate, then the penetration depth of the device is less likely to accumulate over time.

Despite the assumptions, un-modelled dynamics, and non-linearities, the controller successfully eliminated stiction, while rendering the desired geometry. These uncertainties can be eliminated using either a force sensor, better dynamic model of the device, or tuning of the net force constant. In addition, the impact of these errors is amplified in the experimental results; in real applications the penetration depth and sideways motion will be more subtle. As a result, the controller should accurately render the forces in many haptic simulations.

VII. Conclusions

The lack of haptic feedback is a limiting factor in the field of robotic surgery and surgical simulation. These applications require transparent haptic devices producing a wide range of impedance in a stable and controllable way. To satisfy these requirements we constructed a 3-DOF passive haptic device with a parallel kinematic structure and developed a novel controller aimed at improving its performance.

The novel controller improves the range of forces the device generates and eliminates stiction. By adjusting the force output of individual brakes, the controller eliminates the normal component of the net force perpendicular to the virtual surface. Unlike other documented controllers, it approximates forces using combinations of 1, 2, and 3 actuators. The controller was experimentally validated using six testing scenarios. In these tests, the controller successfully modified the force output of the device resulting in a smooth motion along the given surface. Despite numerous model simplifications, such as the simplified dynamic model of the device and linearized hysteresis, the controller was able to accurately render the desired geometry. Naturally, the device experiences some position error attributed to factors other than the controller function.

The device uses passive actuators with a parallel kinematic structure which has many advantages over conventional haptic devices. Due to the parallel kinematics, the structure of the device is light and rigid. It uses brakes as actuators, therefore, it does not require the use of gearboxes, which harm transparency, making it ideal for operations where transparency is a key requirement, like simulation of laparoscopic procedures. Due to its intrinsic stability, the device can also generate high impedance without the risk of instability. As a result, the device is well suited for rendering virtual fixtures guiding the user towards a target in a safe, and controllable way. This stability of the device also makes it ideal for applications where the surgeon interacts with sensitive tissue like nerves or the brain.

An intrinsic feature of passive haptic devices is their inability to generate active forces. This makes the device less suitable for applications like beating heart surgery, lung operations, or drilling operations, where the virtual environment induces motion on the tools i.e., the environment is active. On the other hand, the impedance range of the device limits the usefulness for specialized procedures, like eye surgery, which involves minimal force-feedback. Lastly, the device has 3 translational DOF which makes the device unsuitable for procedures requiring torque feedback. However, since the

device motion is purely translational, a 3 DOF rotational feedback device can be easily added on the top of the device, like in [41]. In such a case, the proposed controller will function the same as before.

Using the device to render virtual environments requires an accurate force measurement which conventionally is provided by a force sensor. Using a more accurate force input estimation can aid in eliminating the plane penetration. Since force sensors are heavy and expensive a force observer could be implemented to estimate the force input of the user without introducing additional mass. Additionally, the dynamic range of the device could be improved by using magnetorheological (MR) brakes that have lower off-state torque and a higher torque output capability [19], [21]. Lastly, using a brake and a motor in tandem can either increase the impedance displayable by the device [42], [43] or to compensate inertia, friction, and gravity, improving its transparency. Since the actuators in the system are attached to an immobile base platform, this addition will not increase the apparent mass of the device.

Future work includes further adapting the proposed haptic device to surgical applications such as simulation of surgical procedures and teleoperated robotic surgery, and move towards hybrid actuation techniques combining both active and passive actuators.

REFERENCES

[1] O. A. Van der Meijden and M. P. Schijven, "The value of haptic feedback in conventional and robot-assisted minimal invasive surgery and virtual reality training: a current review," *Surg. Endosc.*, vol. 23, no. 6, pp. 1180–1190, 2009.

[2] G. Hubens *et al.*, "What have we learnt after two years working with the da vinci robot system in digestive surgery?" *Acta Chirurgica Belgica*, vol. 104, no. 6, pp. 609–614, 2004.

[3] M. Kitagawa *et al.*, "Effect of sensory substitution on suture-manipulation forces for robotic surgical systems," *J. Thorac. and Cardiovasc. Surg.*, vol. 129, no. 1, pp. 151–158, 2005.

[4] S. M. Prasad *et al.*, "The effect of robotic assistance on learning curves for basic laparoscopic skills," *Amer. J. Surg.*, vol. 183, no. 6, pp. 702–707, 2002.

[5] G. Ahlberg *et al.*, "Proficiency-based virtual reality training significantly reduces the error rate for residents during their first 10 laparoscopic cholecystectomies," *Amer. J. Surg.*, vol. 193, no. 6, pp. 797–804, 2007.

[6] E. P. Westebring-van der Putten *et al.*, "Haptics in minimally invasive surgery–a review," *Minim. Invasive Ther. & Allied Technol.*, vol. 17, no. 1, pp. 3–16, 2008.

[7] M. K. Chmarra *et al.*, "Force feedback and basic laparoscopic skills," *Surg. Endoscopy*, vol. 22, no. 10, pp. 2140–2148, 2008.

[8] T. Podder *et al.*, "In vivo motion and force measurement of surgical needle intervention during prostate brachytherapy," *Med. Phys.*, vol. 33, no. 8, pp. 2915–2922, 2006.

[9] A. M. Okamura, C. Simone, and M. D. O'leary, "Force modeling for needle insertion into soft tissue," *IEEE Trans Biomed. Eng.*, vol. 51, no. 10, pp. 1707–1716, 2004.

[10] C. Våpenstad *et al.*, "Limitations of haptic feedback devices on construct validity of the lapsim® virtual reality simulator," *Surg. Endoscopy*, vol. 27, no. 4, pp. 1386–1396, 2013.

[11] ——, "Perceiving haptic feedback in virtual reality simulators," *Surg. Endoscopy*, vol. 27, no. 7, pp. 2391–2397, 2013.

[12] ——, "Lack of transfer of skills after virtual reality simulator training with haptic feedback," *Minim. Invasive Ther. & Allied Technol.*, vol. 26, no. 6, pp. 346–354, 2017.

[13] B. Sainsbury *et al.*, "Evaluation of a virtual reality percutaneous nephrolithotomy (PCNL) surgical simulator," *Front. in Robot. and AI*, vol. 6, p. 145, 2019.

[14] J. E. Colgate and G. G. Schenkel, "Passivity of a class of sampled-data systems: Application to haptic interfaces," *J. Robot. Syst.*, vol. 14, no. 1, pp. 37–47, 1997.

[15] M. Peshkin, J. E. Colgate, and C. Moore, "Passive robots and haptic displays based on nonholonomic elements," in *Proc. IEEE Int. Conf. Robot. and Automat.*, vol. 1. IEEE, 1996, pp. 551–556.

[16] M. R. Reed and W. J. Book, "Modeling and control of an improved dissipative passive haptic display," in *Proc. IEEE Int. Conf. Robot. and Automat.*, vol. 1. IEEE, 2004, pp. 311–318.

[17] O. Topçu, Y. Taşcıoğlu, and E. İ. Konukseven, "Modeling and experimental evaluation of a rotary peristaltic magnetorheological fluid device with low off-state torque for haptic interfaces," *J. Brazilian Soc. Mech. Sci. and Eng.*, vol. 40, no. 1, p. 9, 2018.

[18] C. Cho, M. Kim, and J.-B. Song, "Performance analysis of a 2-link haptic device with electric brakes," in *Proc. Symp. Haptic Interfaces for Virtual Environ. and Teleoperated Syst.* IEEE, 2003, pp. 47–53.

[19] C. Rossa *et al.*, "Design considerations for magnetorheological brakes," *IEEE/ASME Trans. Mechatronics*, vol. 19, no. 5, pp. 1669–1680, 2013.

[20] B. Gonenc and H. Gurocak, "Virtual needle insertion with haptic feedback using a hybrid actuator with DC servomotor and MR-brake with hall-effect sensor," *Mechatronics*, vol. 22, no. 8, pp. 1161–1176, 2012.

[21] C. Rossa *et al.*, "Development of a multilayered wide-ranged torque magnetorheological brake," *Smart Mater. and Struct.*, vol. 23, no. 2, p. 025028, 2014.

[22] D. Karnopp, "Computer simulation of stick-slip friction in mechanical dynamic systems," *J. Dyn. Syst., Meas., and Control*, vol. 107, no. 1, pp. 100–103, 1985.

[23] M. Łącki, B. DeBoon, and C. Rossa, "Impact of kinematic structure on the force displayability of planar passive haptic devices," *IEEE Trans. on Haptics*, vol. 13, no. 1, pp. 219–225, 2020.

[24] T. R. Coles, D. Meglan, and N. W. John, "The role of haptics in medical training simulators: A survey of the state of the art," *IEEE Trans. Haptics*, vol. 4, no. 1, pp. 51–66, 2010.

[25] C. G. Corrêa *et al.*, "Haptic interaction for needle insertion training in medical applications: The state-of-the-art," *Medical Eng. & Physics*, 2018.

[26] D. Senkal, H. Gurocak, and E. I. Konukseven, "Passive haptic interface with mr-brakes for dental implant surgery," *Presence: Teleoperators and Virtual Environ.*, vol. 20, no. 3, pp. 207–222, 2011.

[27] T. A. Kern, *Engineering haptic devices: a beginner's guide for engineers*. Springer, 2009.

[28] C. Cho, J.-B. Song, and M. Kim, "Design and control of a planar haptic device with passive actuators based on passive force manipulability ellipsoid (FME) analysis," *J. Robot. Syst.*, vol. 22, no. 9, pp. 475–486, 2005.

[29] ——, "Energy-based control of a haptic device using brakes," *IEEE Trans. Syst., Man, and Cybern.*, vol. 37, no. 2, pp. 341–349, 2007.

[30] R. E. Stamper, "A three degree of freedom parallel manipulator with only translational degrees of freedom," Ph.D. dissertation, Univ. Maryland, 1997.

[31] N. Karbasizadeh *et al.*, "Experimental dynamic identification and model feed-forward control of novint falcon haptic device," *Mechatronics*, vol. 51, pp. 19–30, 2018.

[32] D. J. Block, M. B. Michelotti, and R. S. Sreenivas, "Application of the novint falcon haptic device as an actuator in real-time control," *J. Behavioral Robot.*, vol. 4, no. 3, pp. 182–193, 2013.

[33] J.-P. Merlet, *Parallel Robots*, 2nd ed. Springer Science & Business Media, 2006, vol. 128.

[34] D. J. Block, M. B. Michelotti, and R. S. Sreenivas, "Application of the novint falcon haptic device as an actuator in real-time control," *J. Behavioral Robot.*, vol. 4, no. 3, pp. 182–193, 2013.

[35] S. Amat, S. Busquier, and Á. Magreñán, "Reducing chaos and bifurcations in newton-type methods," in *Abstract and Appl. Anal.*, vol. 2013. Hindawi, 2013.

[36] M. Łącki and C. Rossa, "On the feasibility of multi-degree-of-freedom haptic devices using passive actuators," in *IEEE Int. Conf. Intell. Robots and Syst.*, Nov 2019, pp. 7282–7287.

[37] J. Duffy, *Statics and Kinematics with Applications to Robotics*. Cambridge University Press, 1996.

[38] C. Melchiorri and G. Vassura, "A performance index for -actuated, multi-wire, haptic interfaces," in *Proc. Int. Conf. Robot. and Automat.*, vol. 2. IEEE, 1998, pp. 1026–1031.

[39] C. Cho, M. Kim, and J.-B. Song, "Direct control of a passive haptic device based on passive force manipulability ellipsoid analysis," *Int. J. Control, Automat., and Syst.*, vol. 2, no. 2, pp. 238–246, 2004.

[40] *Magnetic Particle Brake B2*, Placid Industries, [Datasheet]. Available: www.placidindustries.com/wp-content/uploads/downloads/B2-metric-data-sheet.pdf. Accessed Sep, 21, 2019.

[41] S.-R. Kang *et al.*, "Controllable magnetorheological fluid based actuators for 6-degree-of-freedom haptic master applicable to robot-assisted surgery," *Sensors and Actuators*, vol. 279, pp. 649–662, 2018.

[42] C. Rossa, J. Lozada, and A. Micaelli, "Design and control of a dual unidirectional brake hybrid actuation system for haptic devices," *IEEE Trans. Haptics*, vol. 7, no. 4, pp. 442–453, 2014.

[43] B. DeBoon *et al.*, "Differentially-clutched series elastic actuator for robot-aided musculoskeletal rehabilitation," in *Int. Conf. Robot. and Automat.* IEEE, 2019, pp. 1507–1513.